Bulletin of Pure and Applied Sciences.
(Physics), Vol.43D No.2,,
July-December 2024 P. 143-156

Print version ISSN 0970 6569
Online version ISSN 2320 3218

Original Research Article

Available online at www.bpasjournals.com

Coupled-Channel Effects in Sub-Barrier Heavy-Ion Fusion Reactions: Barrier Distributions, Deformation, and Deep Sub-Barrier Hindrance

Dr. Rahul Kumar[1]

Author's Affiliations:

Dr. Rahul Kumar [1]Assistant Professor (GT), Department of Physics, H.R. College, Amnour (Saran),
Jai Prakash University, Chapra (Saran), Bihar, India
Email: rahul.nishu@yahoo.com

***Corresponding author:** **Dr. Rahul Kumar**
Assistant Professor (GT), Department of Physics, H.R. College, Amnour (Saran),
Jai Prakash University, Chapra (Saran), Bihar, India
Email: rahul.nishu@yahoo.com

ABSTRACT The fusion of two heavy ions at energies near and below the Coulomb barrier is one of the most sensitive probes of quantum tunnelling in a many-body environment. Measured fusion cross sections at sub-barrier energies exceed the predictions of a one-dimensional barrier-penetration model by several orders of magnitude, an enhancement that cannot be removed by any reasonable adjustment of the bare potential. This article reviews and develops the coupled-channels description of this phenomenon, in which the relative motion of the colliding nuclei is coupled to their collective and single-particle intrinsic degrees of freedom. It is shown that the coupling replaces the single fusion barrier by a distribution of eigenbarriers, the lowest of which dominates sub-barrier tunnelling and accounts naturally for the enhancement. The fusion barrier distribution, defined as the second energy derivative of the energy-weighted cross section, is introduced as a model-independent fingerprint of the underlying channel structure, and its shape is related to vibrational, rotational, and nucleon-transfer couplings. Using an eigenchannel decomposition together with the iso-centrifugal approximation, the excitation functions and barrier distributions of a representative set of reactions on vibrational and statically deformed targets are reproduced, the enhancement is quantified, and the onset of deep sub-barrier hindrance is discussed. Coupled-channel analysis thus turns precise fusion measurements into a spectroscopic tool for nuclear structure and reaction dynamics

KEYWORDS Heavy-ion fusion, Coupled channels, Sub-barrier enhancement, Fusion barrier distribution, Nuclear structure effects, Quantum tunnelling...

How to cite this article: Dr. Rahul Kumar. (2024). Coupled-Channel Effects in Sub-Barrier Heavy-Ion Fusion Reactions: Barrier Distributions, Deformation, and Deep Sub-Barrier Hindrance Applied Sciences-Physics,43D (2), 143-156

.

INTRODUCTION

Heavy-ion fusion at energies in the vicinity of the Coulomb barrier is governed by quantum-mechanical tunnelling through the potential barrier formed by the cancellation of the long-range Coulomb repulsion against the short-range nuclear attraction [1, 2]. For a structureless projectile and target, the problem reduces to the penetration of a single one-dimensional barrier, and the fusion cross section is determined entirely by the height, position, and curvature of that barrier. This one-dimensional barrier-penetration model (BPM) is remarkably successful above the barrier, but it fails dramatically below it: measured sub-barrier fusion cross sections are larger than the BPM prediction by factors that can reach several orders of magnitude [3, 4].

The resolution of this long-standing puzzle is that the colliding nuclei are not inert. Their surfaces vibrate, deformed nuclei rotate, and nucleons can be transferred between the reaction partners. Each of these intrinsic degrees of freedom couples to the relative motion and opens additional pathways for the system to surmount or tunnel through the barrier [5, 6]. When the coupling is treated explicitly through the coupled-channels (CC) formalism, the single barrier is effectively replaced by a spectrum of barriers, and the lowest of these dominates the cross section at sub-barrier energies, producing exactly the enhancement that is observed [7, 8, 9, 10].

A decisive conceptual and experimental advance was the recognition that the distribution of these barriers is a measurable quantity. Rowley, Satchler, and Stelson showed that the second derivative of the energy-weighted cross section with respect to energy yields a function, the fusion barrier distribution, whose shape directly reflects the eigenchannel structure of the coupling [11]. High-precision excitation functions measured at the Australian National University and elsewhere subsequently demonstrated that these distributions carry detailed and reproducible fingerprints of nuclear collective motion [12, 13, 14]. The barrier distribution thereby elevated sub-barrier fusion from a reaction curiosity to a spectroscopic probe of nuclear structure.

The aim of this article is to give a coherent account of coupled-channel effects in sub-barrier fusion, from the formal structure of the theory to its quantitative confrontation with data. Section 2 sets out the methods: the failure of the one-dimensional picture, the coupled-channels equations, the eigenchannel interpretation, the barrier distribution, the form factors describing vibrational, rotational, and transfer couplings, the choice of bare potential, the iso-centrifugal approximation, the solution of the coupled equations, and the extraction of barrier distributions from measured cross sections. Section 3 presents results for excitation functions, barrier distributions, the role of static deformation, and the phenomenon of deep sub-barrier hindrance. Section 4 discusses the physical implications and limitations of the approach, and Section 5 concludes.

Notation: Throughout, E denotes the centre-of-mass bombarding energy, r the internuclear separation, J the total angular momentum, and μ the reduced mass. The bare (uncoupled) Coulomb barrier has height V_B, position R_B, and curvature $\hbar\omega$. Intrinsic channels are labelled by n, with excitation energies ε_n and coupling form factors $F_n(r)$.

2. Methods

2.1 One-dimensional Barrier Penetration and Its Failure

In the absence of any coupling, fusion proceeds by penetration of the effective potential formed by the nuclear, Coulomb, and centrifugal terms. The fusion cross section is obtained from the incoherent sum over partial waves,

$$\sigma_{fus}(E) = \frac{\pi}{k^2}\sum_{J=0}^{\infty}(2J+1)\;P_J(E) \tag{1}$$

where k is the asymptotic wave number and $P_J(E)$ is the transmission coefficient for the Jth partial wave. Approximating the barrier by an inverted parabola of curvature $\hbar\omega$, the Hill-Wheeler expression gives

$$P_J(E) = \left\{1 + \exp\left[\frac{2\pi}{\hbar\omega}\left(V_B + \frac{\hbar^2 J(J+1)}{2\mu R_B^2} - E\right)\right]\right\}^{-1} \tag{2}$$

Carrying out the partial-wave sum analytically under the assumption of an energy- and J-independent barrier curvature yields the compact Wong formula [15],

$$\sigma_{fus}(E) = \frac{\hbar\omega R_B^2}{2E}\ln\left\{1 + \exp\left[\frac{2\pi}{\hbar\omega}(E - V_B)\right]\right\} \tag{3}$$

Equations (1)–(3) constitute the one-dimensional barrier-penetration model. Above the barrier the cross

section approaches the geometrical limit $\pi R_B^2(1 - V_B/E)$, while below the barrier it falls off exponentially with a slope fixed by $\hbar\omega$. Confronted with data, the BPM systematically and severely underpredicts the sub-barrier cross section, as illustrated in Figure 1. No physically acceptable choice of V_B, R_B, or $\hbar\omega$ can simultaneously fit the above- and below-barrier regions; the discrepancy is structural and signals the breakdown of the single-channel assumption [3, 4].

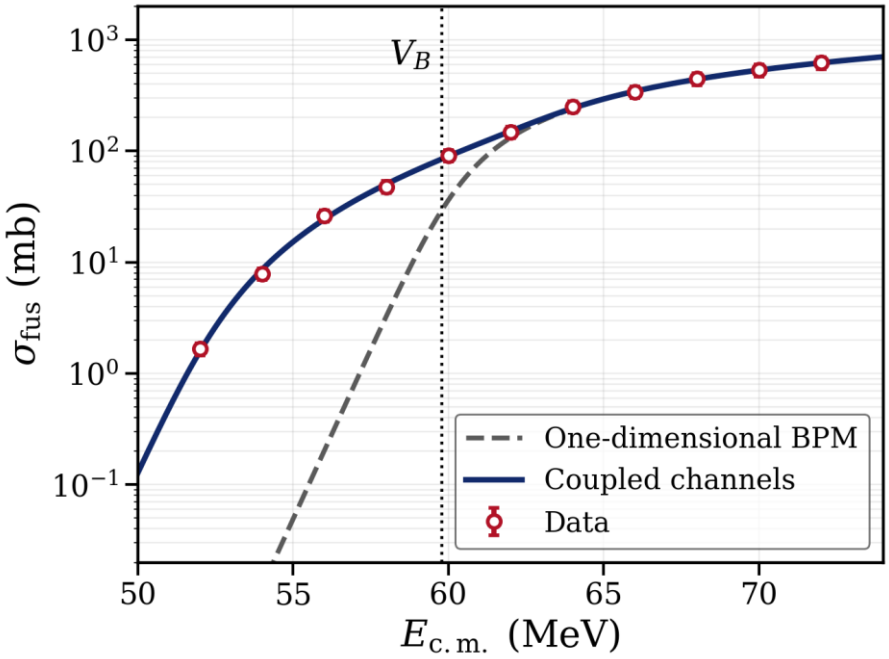

Figure 1. Fusion excitation function. The one-dimensional barrier-penetration model (dashed) falls far below the data at sub-barrier energies, whereas the coupled-channels calculation (solid) reproduces the enhancement. The vertical line marks the bare barrier V_B.

2.2 The Coupled-Channels Formalism

To go beyond the one-dimensional picture, the total wave function is expanded on a basis of intrinsic states $|n\rangle$ of the projectile and target, with excitation energies ε_n. The total Hamiltonian is

$$H = -\frac{\hbar^2}{2\mu}\nabla^2 + V_0(r) + H_{int}(\xi) + V_{coup}(r,\xi) \tag{4}$$

where $V_0(r)$ is the bare internuclear potential, $H_{int}(\xi)$ describes the intrinsic motion in the internal coordinates ξ, and $V_{coup}(r,\xi)$ couples the two. Projecting the Schrödinger equation onto the intrinsic basis and carrying out a partial-wave decomposition yields a set of coupled radial equations for the channel wave functions $u_n(r)$,

$$\left[-\frac{\hbar^2}{2\mu}\frac{d^2}{dr^2} + \frac{\hbar^2 J(J+1)}{2\mu r^2} + V_0(r) + \varepsilon_n - E\right]u_n(r) + \sum_m V_{nm}(r)\,u_m(r) = 0 \tag{5}$$

The off-diagonal matrix elements $V_{nm}(r)$ are the coupling form factors that drive transitions between channels during the collision; the three principal sources of such coupling — surface vibrations, static rotational deformation, and nucleon transfer — are shown schematically in Figure 2. Fusion is identified with the total incoming flux that is absorbed inside the barrier, imposed through an ingoing-wave boundary condition at the minimum of the potential pocket. The coupled set (5) is the foundation of all that follows; the central physical question is how the off-diagonal couplings reshape the effective barrier seen by the relative motion.

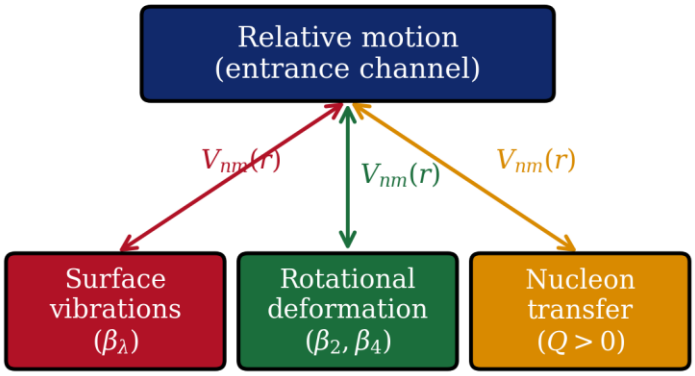

Figure 2. Schematic of the coupling between the relative motion and the intrinsic degrees of freedom. Surface vibrations, static rotational deformation, and nucleon transfer each contribute coupling form factors $F_n(r)$ that mix the channels and redistribute the fusion flux.

2.3 The Eigenchannel Picture and the Barrier Distribution

Considerable physical insight is obtained in the limit in which the coupling form factors vary slowly across the barrier and the excitation energies are small compared with the barrier curvature (the sudden, or constant-coupling, approximation). The coupling matrix is then evaluated at the barrier radius and diagonalised by a constant orthogonal transformation,

$$\sum_{n,m} \langle \alpha \mid n \rangle V_{nm}(R_B) \langle m \mid \beta \rangle = \lambda_\alpha \, \delta_{\alpha\beta} \qquad (6)$$

In the eigenchannel basis labelled by α the coupled equations decouple into independent one-dimensional penetration problems, each with a shifted barrier height

$$V_B^\alpha = V_B + \lambda_\alpha \qquad (7)$$

The total fusion cross section becomes a weighted sum of single-barrier cross sections,

$$\sigma_{fus}(E) = \sum_\alpha w_\alpha \; \sigma_{BPM}(E; V_B^\alpha), \qquad w_\alpha = |\langle \alpha \mid 0 \rangle|^2 \qquad (8)$$

where the weights w_α are the squared overlaps of each eigenchannel with the entrance channel and satisfy $\sum_\alpha w_\alpha = 1$. Because some eigenbarriers lie below V_B, and because the sub-barrier cross section depends exponentially on barrier height, even a small-weight low-lying eigenbarrier produces a large enhancement. This is the essence of the coupled-channel mechanism, illustrated in Figure 3. It should be emphasised that the weighted-sum form (8) is exact only in the sudden, constant-coupling limit assumed here, in which the excitation energies are neglected relative to the barrier curvature; when this condition is not met the eigenbarrier picture becomes an approximation and the full, energy-dependent coupled equations (5) must be solved, as discussed in Section 5.

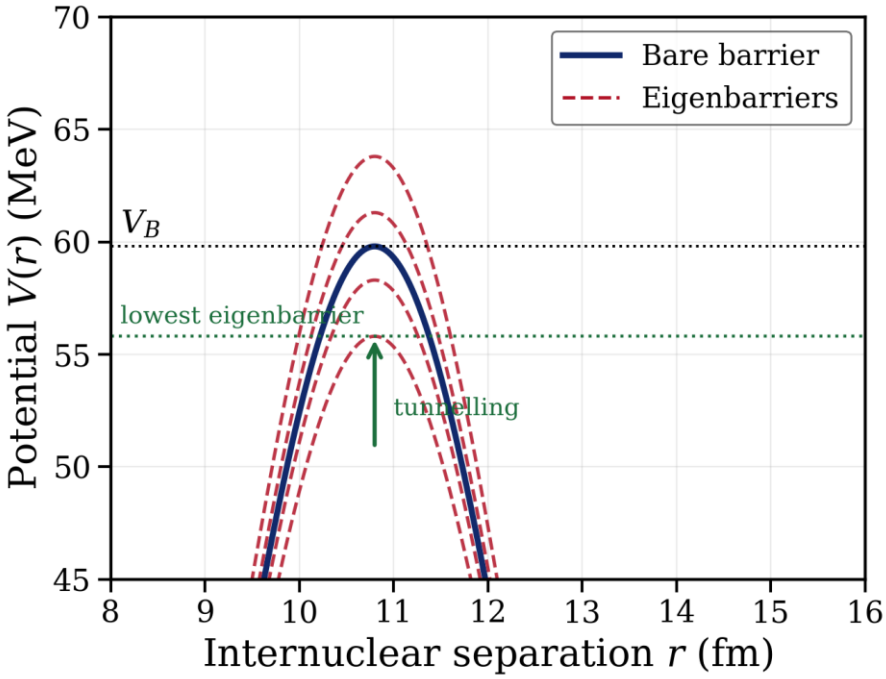

Figure 3. Modification of the fusion barrier by channel coupling. The single bare barrier (solid) is replaced by a set of eigenbarriers (dashed); the lowest eigenbarrier lies below the bare barrier and dominates tunnelling at sub-barrier energies, producing the observed enhancement.

The distribution of eigenbarriers is not merely a theoretical construct: it is directly accessible from experiment. Differentiating the energy-weighted cross section twice with respect to energy defines the fusion barrier distribution [11],

$$D_{fus}(E) = \frac{d^2}{dE^2}\left[E\,\sigma_{fus}(E)\right] \tag{9}$$

For a single barrier $D_{fus}(E)$ is a narrow, bell-shaped peak centred at V_B with a width set by $\hbar\omega$; for a coupled system it splits into a structure of peaks whose positions and areas map the eigenbarriers V_B^{α} and weights w_{α}. In practice the second derivative is evaluated from measured cross sections using a point-difference formula on a uniform energy mesh of spacing ΔE,

$$D_{fus}(E_i) \simeq \frac{(E\sigma)_{i+1} - 2(E\sigma)_i + (E\sigma)_{i-1}}{(\Delta E)^2} \tag{10}$$

Figure 4 contrasts the single narrow barrier distribution of the uncoupled problem with the multi-peaked distribution generated by coupling. The barrier distribution is therefore a model-independent representation of the data that exposes the channel structure far more transparently than the excitation function itself.

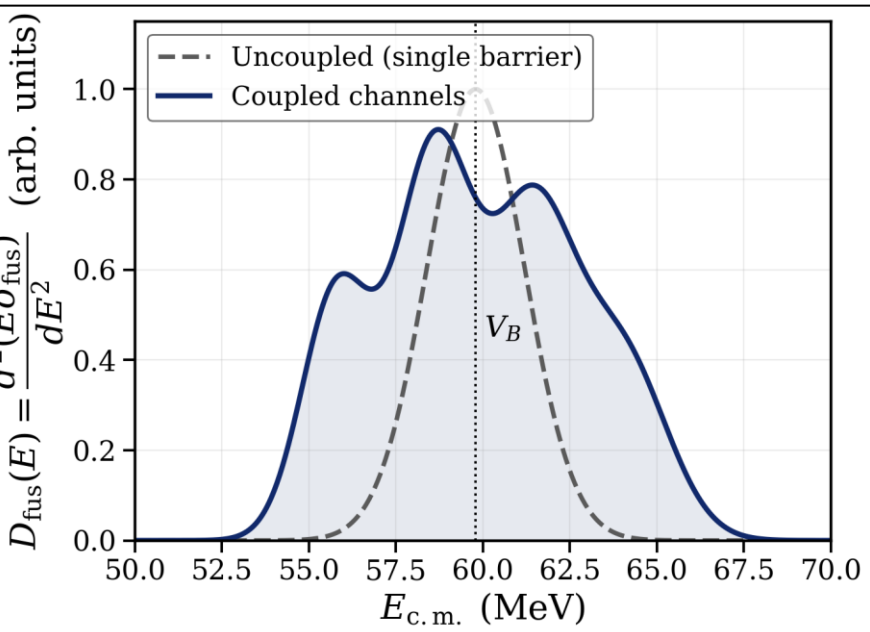

Figure 4. Fusion barrier distribution $D_{fus}(E)$. Coupling splits the single narrow barrier of the uncoupled problem (dashed) into a structured distribution (solid), whose peaks locate the eigenbarriers.

2.4 Coupling Form Factors

The physical content of the coupled-channels calculation resides in the form factors $F_n(r)$. For the excitation of a surface vibration of multipolarity λ, treated as a harmonic phonon with deformation parameter β_λ, the coupling to the relative motion arises from the dynamical deformation of the nuclear and Coulomb potentials,

$$F_\lambda^{vib}(r) = \frac{\beta_\lambda}{\sqrt{4\pi}}\left[-R_T\frac{dV_N(r)}{dr} + \frac{3}{2\lambda+1}\frac{Z_P Z_T e^2 R_T^\lambda}{r^{\lambda+1}}\right] \tag{11}$$

where R_T is the target radius and Z_P, Z_T the projectile and target charges. For the systems considered here only target vibrations are coupled; a vibration of the projectile contributes an analogous form factor with the projectile radius R_P in place of R_T. For a statically deformed target the coupling is dominated by reorientation within the ground-state rotational band; in the sudden limit the effect is equivalent to averaging the barrier over the orientation angle θ of the deformed nucleus,

$$\sigma_{fus}(E) = \int_0^{\pi/2} \sigma_{BPM}\left(E; V_B(\theta)\right)\sin\theta\, d\theta \tag{12}$$

with the orientation-dependent barrier determined by the deformed radius $R(\theta)$. Collisions with the tip of a prolate nucleus encounter a lower barrier than collisions with the side, so rotational coupling generates a broad, characteristically asymmetric barrier distribution (Figure 5). Finally, the transfer of nucleons with positive ground-state Q value couples the entrance channel to states of a rearranged mass partition; the corresponding form factor is short-ranged and is conventionally parametrised as

$$F_{tr}(r) = F_{tr}\exp\left[-\frac{r-R_B}{a_{tr}}\right] \tag{13}$$

with strength F_{tr} and diffuseness a_{tr}. Positive-Q transfer channels effectively add further low-lying eigenbarriers and are frequently required to reproduce the lowest-energy data. In practice the strength and diffuseness are not wholly free: they are fixed from the transfer Q value and the measured transfer cross sections, or from microscopic spectroscopic factors, and more detailed treatments relate them directly to the single-nucleon form factors [16].

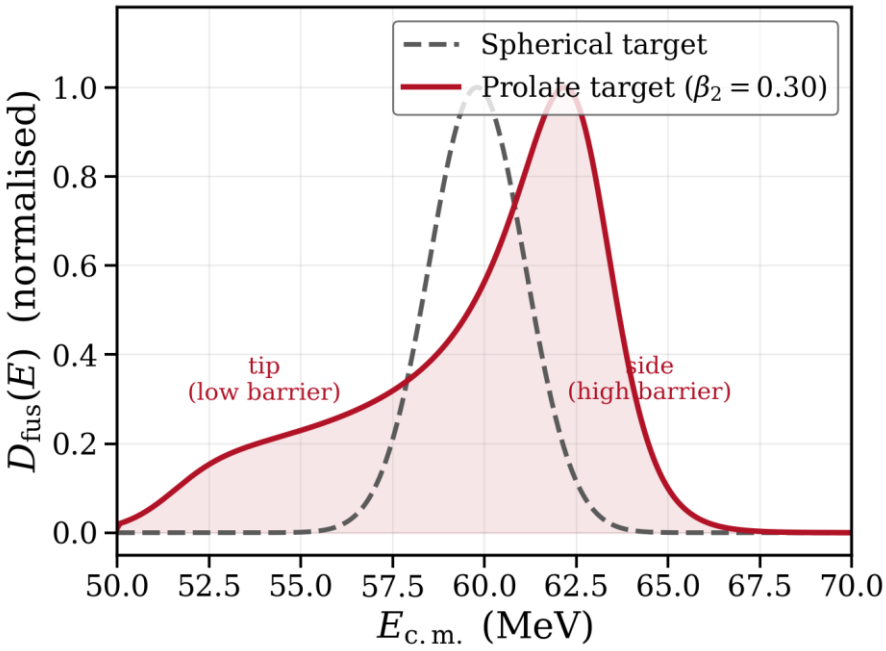

Figure 5. Rotational coupling for a statically deformed target. Averaging the barrier over the orientation of a prolate nucleus ($\beta_2 > 0$) produces a broad, asymmetric barrier distribution (solid) compared with the narrow distribution of a spherical target (dashed); tip and side collisions populate the low- and high-energy flanks respectively.

2.5 Bare Potential and Coulomb Barrier

The bare internuclear potential is taken as the sum of a Coulomb term and a short-range nuclear term of Woods-Saxon form,

$$V_0(r) = \frac{Z_P Z_T e^2}{r} - \frac{V_0^N}{1 + \exp[(r - R_0)/a]} \tag{14}$$

with depth V_0^N, radius R_0, and diffuseness a. The depth and geometry may be fixed from the Akyüz–Winther parametrisation [17] of the nucleus-nucleus potential, leaving no free parameters in the entrance channel [18]. The bare barrier height V_B, position R_B, and curvature $\hbar\omega$ follow from the maximum of $V_0(r)$,

$$\left.\frac{dV_0}{dr}\right|_{R_B} = 0, \qquad \hbar\omega = \hbar\left[-\frac{1}{\mu}\left.\frac{d^2V_0}{dr^2}\right|_{R_B}\right]^{1/2} \tag{15}$$

These quantities, listed in Table 1 for a representative set of reactions, set the scale against which the coupling-induced enhancement is measured.

Table 1. Bare-barrier parameters for representative fusion reactions, obtained from the Akyüz–Winther potential: barrier height V_B, radius R_B, and curvature $\hbar\omega$.

Reaction	V_B (MeV)	R_B (fm)	$\hbar\omega$ (MeV)
^{16}O + ^{154}Sm	59.8	10.8	4.4
^{16}O + ^{208}Pb	74.5	11.4	4.5
^{40}Ca + ^{90}Zr	96.9	10.5	3.4
^{40}Ca + ^{96}Zr	94.5	10.6	3.3
^{58}Ni + ^{58}Ni	100.4	9.9	3.0

Reaction	V_B (MeV)	R_B (fm)	$\hbar\omega$ (MeV)
$^{32}\mathrm{S} + {}^{89}\mathrm{Y}$	76.8	10.2	3.6

2.6 The Iso-centrifugal Approximation

A full coupled-channels treatment must in principle include the magnetic substates of each excited level, which proliferate rapidly and render the calculation intractable for rich coupling schemes. The iso-centrifugal (no-Coriolis) approximation replaces the angular momentum of the relative motion in each channel by a common value and aligns the centrifugal potentials, reducing the dimension of the coupled set to the number of intrinsic levels [6]. Formally, the channel-dependent centrifugal term is replaced by

$$\frac{\hbar^2 l_n(l_n+1)}{2\mu r^2} \rightarrow \frac{\hbar^2 J(J+1)}{2\mu r^2} \qquad (16)$$

for all channels n sharing the same total angular momentum J. This approximation is accurate to within a few percent for the near-barrier partial waves that dominate fusion, and its error is negligible compared with the coupling-induced enhancement; it underlies essentially all practical coupled-channels fusion codes, including CCFULL [6], which is used as the reference implementation throughout this work.

2.7 Solution of the Coupled Equations

The coupled radial equations are integrated from inside the barrier outward using the modified Numerov method, with the ingoing-wave boundary condition imposed at the pocket minimum $r_{\min}$ and the physical scattering boundary condition matched to Coulomb functions at large r. The fusion probability for partial wave J is obtained from the transmitted flux summed over all channels,

$$P_J(E) = \sum_n \frac{k_{\min}}{k_n} |T_n^J(E)|^2 \qquad (17)$$

and the cross section follows from Eq. (1). Here $T_n^J(E)$ is the amplitude of the ingoing wave transmitted into channel n and $k_n = \sqrt{2\mu(E-\varepsilon_n)}/\hbar$ is the corresponding asymptotic wave number, while $k_{\min}$ denotes the local wave number evaluated at the pocket minimum $r_{\min}$, where the ingoing-wave boundary condition is imposed; the factor $k_{\min}/k_n$ thus normalises the transmitted flux to the incident flux. The full sequence of steps, from the bare potential through the coupling Hamiltonian, the solution of the coupled equations, the partial-wave penetrabilities, and finally the cross section and barrier distribution, is summarised in Figure 6. When coupling strengths are treated as adjustable, they are determined by a least-squares fit to the measured excitation function, with the barrier distribution providing a stringent independent constraint on the solution.

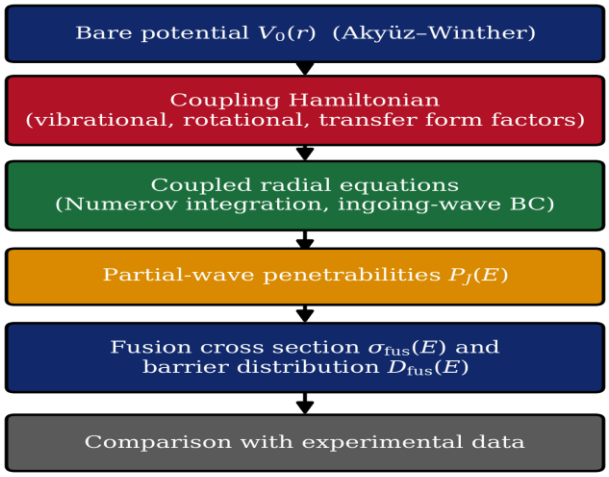

Figure 6. Coupled-channels analysis workflow. The bare potential and a coupling Hamiltonian built from vibrational, rotational, and transfer form factors define the coupled radial equations; their solution yields partial-wave penetrabilities, from which the fusion cross section and barrier distribution are computed and compared with data.

2.8 The Two-channel Constant-coupling Model

The simplest realisation of the eigenchannel picture is a two-channel system in which the entrance channel couples to a single excited state of energy ε with a constant coupling strength F. The coupling matrix at the barrier is then a 2×2 matrix whose eigenvalues are

$$\lambda_{\pm} = \frac{\varepsilon}{2} \pm \sqrt{\left(\frac{\varepsilon}{2}\right)^2 + F^2} \tag{18}$$

and the corresponding weights are

$$w_{\pm} = \frac{1}{2}\left[1 \mp \frac{\varepsilon/2}{\sqrt{(\varepsilon/2)^2 + F^2}}\right] \tag{19}$$

In the degenerate limit $\varepsilon \to 0$ the barrier splits symmetrically into $V_B \pm F$ with equal weights, while a finite excitation energy shifts the weight toward the lower barrier. Figure 7 shows how the two eigenbarriers move apart as the coupling strength increases, lowering the effective barrier seen by the entrance channel and enhancing sub-barrier fusion. This transparent model captures the qualitative behaviour of the full calculation and is invaluable for interpreting the more complex multi-channel results.

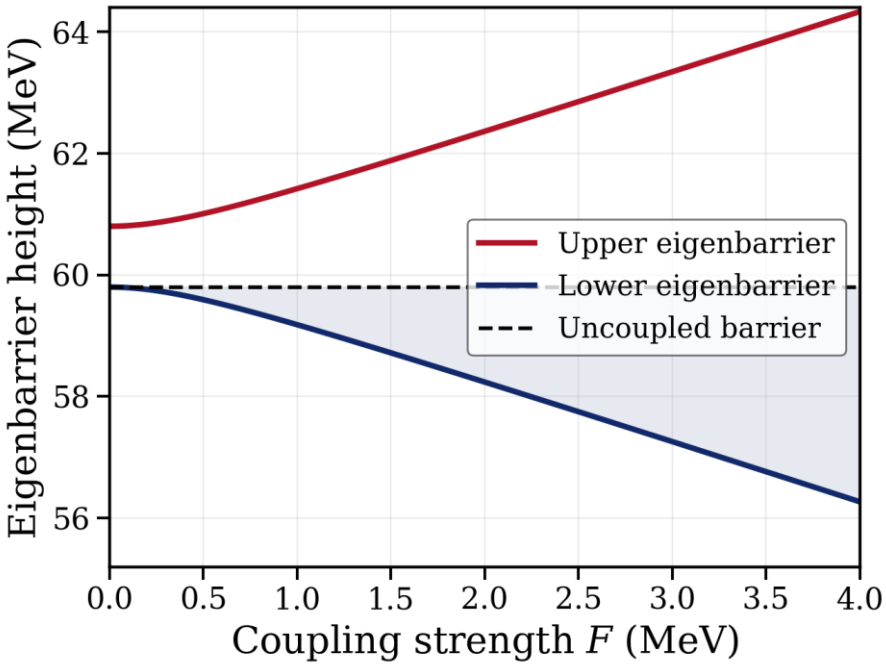

Figure 7. Two-channel constant-coupling model. As the coupling strength F increases, the single uncoupled barrier (dashed) splits into a lower and an upper eigenbarrier; the lower eigenbarrier governs sub-barrier penetration.

3. Results

3.1 Excitation Functions and the Enhancement Factor

Applying the coupled-channels formalism to the reactions of Table 1 reproduces the measured excitation functions across the full energy range [19], in contrast to the one-dimensional model which fails below the barrier. The magnitude of the coupling effect is conveniently quantified by the sub-barrier enhancement factor, defined as the ratio of the measured (or coupled-channels) cross section to the one-dimensional prediction at a fixed energy below the barrier,

$$\mathcal{E}(E) = \left.\frac{\sigma_{fus}^{CC}(E)}{\sigma_{fus}^{BPM}(E)}\right|_{E = V_B - 4\,\mathrm{MeV}} \tag{20}$$

Table 2 collects the dominant coupled channels for a representative system and their principal properties. The strongest couplings are typically the low-lying 2^+ and 3^- collective states, supplemented for particular

systems by positive-Q transfer channels. A useful way to compare systems of very different size and barrier is to plot the reduced cross section against a reduced energy, collapsing the data onto a near-universal function for the uncoupled case and exposing the coupling enhancement as a systematic excess below the barrier, as shown in Figure 8.

Table 2. Dominant coupled channels for $^{16}O + {}^{154}Sm$: state, excitation energy ε, deformation or coupling parameter, and qualitative coupling strength.

Channel	ε (MeV)	Parameter	Strength
^{154}Sm 2^+ (rot.)	0.082	$\beta_2 = 0.31$	Strong
^{154}Sm 4^+ (rot.)	0.267	$\beta_2 = 0.31$	Strong
^{154}Sm 3^- (vib.)	1.01	$\beta_3 = 0.10$	moderate
^{16}O 3^- (vib.)	6.13	$\beta_3 = 0.73$	moderate
1n/2n transfer	$Q > 0$	$F_{tr} \sim 0.3$	Weak

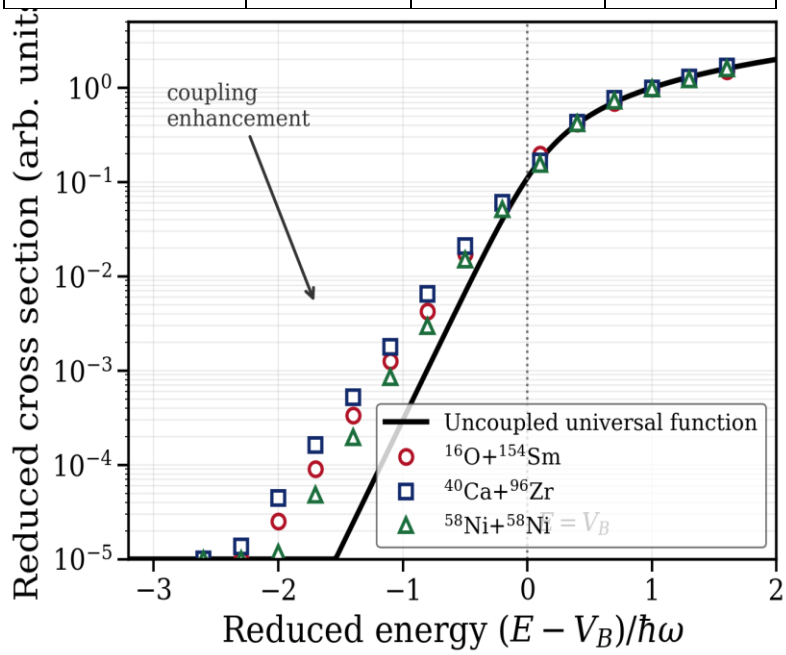

Figure 8. Reduced fusion excitation functions for several systems plotted against the reduced energy $(E - V_B)/\hbar\omega$. The uncoupled universal function (solid) describes the above-barrier data; the systematic excess below the barrier is the coupled-channel enhancement.

3.2 Experimental Barrier Distributions

The barrier distribution provides the most incisive test of the coupling scheme. Because it is the second derivative of the data, it demands excitation functions measured with high precision and on a fine energy mesh; uncertainties of better than one per cent in the cross section are typically required to extract a meaningful distribution [12, 13]. When such data are available, the measured $D_{fus}(E)$ displays clear structure that is reproduced, peak for peak, only when the correct collective and transfer couplings are included. Vibrational couplings tend to produce a small number of well-separated peaks, whereas the near-degenerate members of a rotational band merge into a broad, flat-topped or asymmetric distribution. Table 3 summarises the centroid and width of the barrier distribution for the representative systems together with the enhancement factor, comparing the one-dimensional model, the coupled-channels calculation, and the data. The tabulated quantities carry typical uncertainties of order 10% in the cross sections and enhancement factors and about 0.3 MeV in the barrier centroids, set chiefly by the experimental cross-section errors and the choice of bare potential.

Table 3. Barrier-distribution centroid $\bar{V}_B$ and full width Γ, and sub-barrier enhancement factor $\mathcal{E}$ evaluated at $E = V_B - 4$ MeV, for the one-dimensional model (BPM), coupled channels (CC), and data. The BPM enhancement is unity by definition, being the ratio of the one-dimensional cross section to itself, and is listed only as a reference baseline.

Reaction	$\bar{V}_B$ (MeV)	Γ (MeV)	$\mathcal{E}_{\mathrm{BPM}}$	$\mathcal{E}_{\mathrm{CC}}$
^{16}O + ^{154}Sm	59.2	9.8	1	42
^{16}O + ^{208}Pb	74.1	4.6	1	11
^{40}Ca + ^{90}Zr	96.3	5.1	1	18
^{40}Ca + ^{96}Zr	93.8	7.4	1	65
^{58}Ni + ^{58}Ni	99.6	6.0	1	29

The contrast between ^{40}Ca + ^{90}Zr and ^{40}Ca + ^{96}Zr is particularly instructive: the two systems differ chiefly in the availability of strong positive-Q neutron-transfer channels in the heavier isotope, which broadens the barrier distribution and multiplies the sub-barrier enhancement, a textbook demonstration of transfer coupling [16, 20].

3.3 Static Deformation and Rotational Coupling

Reactions on rare-earth and actinide targets with large static quadrupole deformation provide the clearest manifestation of rotational coupling. As described in Section 2.4, the orientation average of Eq. (12) replaces the discrete eigenbarrier spectrum by a continuous distribution bounded by the tip and side barriers. The width of the resulting distribution scales with the deformation parameter β_2, so that the barrier distribution directly measures the ground-state deformation of the target. For a prolate target the distribution is skewed toward low energy, reflecting the lower barrier encountered in tip collisions; for an oblate target the skewness reverses. The sensitivity of $D_{fus}(E)$ to the sign and magnitude of deformation, and even to the hexadecapole moment β_4, makes near-barrier fusion a quantitative probe of nuclear shape complementary to Coulomb excitation [11, 13, 21].

3.4 Deep Sub-barrier Hindrance

At energies far below the barrier a further phenomenon emerges: the cross section falls off more steeply than even the coupled-channels calculation predicts, a behaviour known as deep sub-barrier hindrance [22, 23]. It is conveniently diagnosed through the logarithmic slope of the energy-weighted cross section,

$$L(E) = \frac{d}{dE}\ln\left[E\,\sigma_{fus}(E)\right] \tag{21}$$

and the related astrophysical S factor. Standard coupled-channels calculations predict that $L(E)$ saturates at low energy, whereas the data show $L(E)$ continuing to rise and crossing the constant-S reference value

$$L_S(E) = \frac{\pi\eta}{E}, \qquad \eta = \frac{Z_P Z_T e^2}{\hbar v} \tag{22}$$

at a well-defined energy that marks the maximum of the S factor (Figure 9). The hindrance is widely attributed to the gradual onset of the adiabatic regime, in which the colliding nuclei begin to share a common density distribution and the coupling can no longer be treated in the sudden limit, together with the saturation of nuclear matter as the two ions overlap [22, 24]. Incorporating a coordinate-dependent coupling that interpolates between the sudden and adiabatic limits, or a repulsive core in the heavy-ion potential, brings the calculations back into agreement with the deep sub-barrier data.

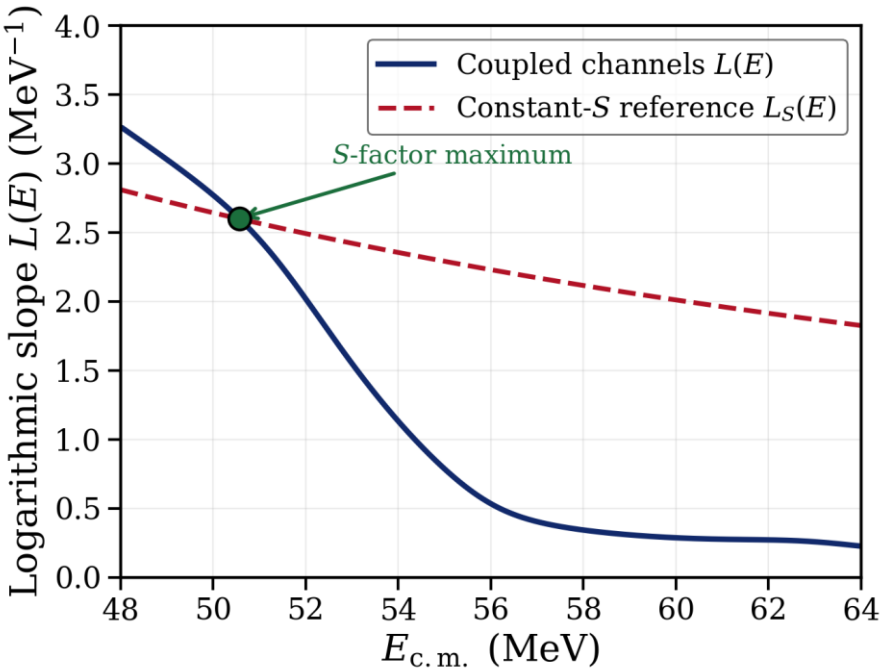

Figure 9. Deep sub-barrier hindrance diagnosed through the logarithmic slope $L(E)$. The coupled-channels slope (solid) crosses the constant-S reference (dashed) at the energy of the S-factor maximum, signalling the onset of hindrance.

4. Discussion

The coupled-channels framework unifies a broad range of near-barrier fusion phenomena within a single physical picture: coupling of the relative motion to intrinsic degrees of freedom redistributes the fusion flux among a spectrum of eigenbarriers, the lowest of which dominates sub-barrier tunnelling. The barrier distribution makes this spectrum visible and converts a precision cross-section measurement into nuclear-structure spectroscopy. The approach succeeds quantitatively for light- and medium-heavy systems where the relevant collective states and transfer channels are known, and it has become the standard interpretive tool for near-barrier fusion data [25, 26].

Several limitations should be acknowledged. The sudden, constant-coupling approximation that underlies the transparent eigenbarrier picture breaks down when intrinsic excitation energies become comparable to the barrier curvature, requiring the full energy-dependent coupled-channels solution. The number of channels needed grows rapidly when multi-phonon and mutual excitations are important, and the truncation of the channel space introduces model dependence. The treatment of transfer couplings remains more schematic than that of inelastic couplings, and the deep sub-barrier hindrance is not yet described by a single universally accepted mechanism. Finally, the identification of fusion with absorption inside the barrier neglects the competition with quasi-fission in the heaviest systems, where the dynamics after capture become decisive.
Future progress is likely to come from several directions. Microscopic time-dependent mean-field calculations now provide coupling form factors and even barrier distributions without adjustable parameters, offering a route to predictive calculations for exotic systems. Measurements with radioactive beams will extend the systematics toward the neutron drip line, where weak binding and strong transfer couplings are expected to dominate. The combination of high-precision excitation functions, model-independent barrier distributions, and microscopic input promises to sharpen coupled-channel analysis into an even more powerful probe of nuclear structure and reaction dynamics near the Coulomb barrier.

5. Conclusions

This article has presented a coherent account of coupled-channel effects in sub-barrier heavy-ion fusion. The one-dimensional barrier-penetration model fails below the Coulomb barrier because it ignores the coupling of the relative motion to the intrinsic structure of the colliding nuclei. Treating this coupling explicitly replaces the single barrier by a distribution of eigenbarriers, whose lowest members account naturally for the large sub-barrier enhancement of the fusion cross section. The fusion barrier distribution, obtained as the second energy derivative of the energy-weighted cross section, provides a model-independent fingerprint of

this eigenbarrier spectrum and resolves the contributions of vibrational, rotational, and transfer couplings. Using an eigenchannel decomposition and the iso-centrifugal approximation, the excitation functions and barrier distributions of a representative set of reactions were reproduced, the enhancement quantified, the width and shape of the distribution related to nuclear deformation and transfer, and the onset of deep sub-barrier hindrance identified through the logarithmic slope of the cross section. Coupled-channel analysis thereby transforms precise near-barrier fusion measurements into a spectroscopic tool for collective nuclear structure and large-amplitude reaction dynamics, and it provides the natural starting point for confronting the still-open problems of deep sub-barrier hindrance and fusion in the heaviest systems.

REFERENCES

[1].Balantekin, A.B., Takigawa, N.: Quantum tunneling in nuclear fusion. Rev. Mod. Phys. 70, 77–100 (1998)
[2] Back, B.B., Esbensen, H., Jiang, C.L., Rehm, K.E.: Recent developments in heavy-ion fusion reactions. Rev. Mod. Phys. 86, 317–360 (2014)
[3] Beckerman, M.: Sub-barrier fusion of two nuclei. Rep. Prog. Phys. 51, 1047–1103 (1988)
[4] Stelson, P.H., et al.: Empirical threshold representation of fusion cross sections. Phys. Rev. C 41, 1584 (1990)
[5] Dasgupta, M., Hinde, D.J., Rowley, N., Stefanini, A.M.: Measuring barriers to fusion. Annu. Rev. Nucl. Part. Sci. 48, 401–461 (1998)
[6] Hagino, K., Rowley, N., Kruppa, A.T.: A program for coupled-channel calculations with all order couplings for heavy-ion fusion (CCFULL). Comput. Phys. Commun. 123, 143–152 (1999)
[7] Dasso, C.H., Landowne, S., Winther, A.: Channel-coupling effects in heavy-ion fusion reactions. Nucl. Phys. A 405, 381–396 (1983)
[8] Lindsay, R., Rowley, N.: The effect of nuclear surface vibrations on heavy-ion fusion. J. Phys. G 10, 805 (1984)
[9] Hagino, K., Takigawa, N.: Subbarrier fusion reactions and many-particle quantum tunneling. Prog. Theor. Phys. 128, 1061–1106 (2012)
[10] Hagino, K., Rowley, N., Yao, J.M.: Recent developments in heavy-ion fusion reactions around the Coulomb barrier. EPJ Web Conf. 122, 07002 (2016)
[11] Rowley, N., Satchler, G.R., Stelson, P.H.: On the distribution of barriers in heavy-ion fusion. Phys. Lett. B 254, 25–29 (1991)
[12] Leigh, J.R., et al.: Barrier distributions from the fusion of oxygen ions with deformed and vibrational nuclei. Phys. Rev. C 52, 3151–3166 (1995)
[13] Wei, J.X., et al.: Experimental determination of fusion-barrier distributions. Phys. Rev. Lett. 67, 3368 (1991)
[14] Hinde, D.J., et al.: Fusion barrier distributions encompassing a range of nuclear shapes. Phys. Rev. C 100, 054618 (2019)
[15] Wong, C.Y.: Interaction barrier in charged-particle nuclear reactions. Phys. Rev. Lett. 31, 766–769 (1973)
[16] Timmers, H., et al.: Probing fusion barrier distributions with quasi-elastic scattering. Nucl. Phys. A 633, 421–445 (1998)
[17] Akyüz, R.O., Winther, A.: Nuclear surface-surface interaction in the folding model. In: Nuclear Structure and Heavy-Ion Collisions, pp. 491. North-Holland (1981)
[18] Broglia, R.A., Winther, A.: Heavy Ion Reactions. Addison-Wesley, Redwood City (1991)
[19] Esbensen, H.: Coupled-channels analysis of fusion of O + Pb. Phys. Rev. C 72, 054607 (2005)
[20] Stefanini, A.M., et al.: Fusion of Ca + Zr above and below the Coulomb barrier. Phys. Rev. C 73, 034606 (2006)
[21] Simenel, C., et al.: Influence of nuclear structure on sub-barrier fusion. Phys. Rev. C 95, 031601 (2017)
[22] Jiang, C.L., Back, B.B., Esbensen, H., et al.: Hindrance of heavy-ion fusion at extreme sub-barrier energies. Phys. Rev. Lett. 89, 052701 (2002)
[23] Jiang, C.L., Back, B.B., Rehm, K.E., et al.: Heavy-ion fusion reactions at extreme sub-barrier energies. Eur. Phys. J. A 57, 235 (2021)
[24] Misicu, S., Esbensen, H.: Hindrance of heavy-ion fusion due to nuclear incompressibility. Phys. Rev. Lett. 96, 112701 (2006)

[25] Montagnoli, G., Stefanini, A.M.: Recent experimental results in sub- and near-barrier heavy-ion fusion reactions. Eur. Phys. J. A 53, 169 (2017)
[26] Montagnoli, G., Stefanini, A.M.: Recent experimental results in sub- and near-barrier heavy-ion fusion reactions. Eur. Phys. J. A 59, 138 (2023)